

# Polyvinyl Acetate-Based Polymer Host for Optical and Far-Infrared Spectroscopy of Individualized Nanoparticles

Henry V. Wladkowski,<sup>1</sup> Julian Duarte,<sup>1</sup> Shashank R. Nandyala,<sup>2</sup> Joshua S. Walker,<sup>1</sup> Subash Kattel,<sup>1</sup> Jeffrey L. Blackburn,<sup>3</sup> Jeffrey A. Fagan,<sup>4</sup> Jon M. Pikal,<sup>2</sup> and William D. Rice\*<sup>1</sup>

<sup>1</sup>*Department of Physics & Astronomy, University of Wyoming, Laramie, WY, 82071*

<sup>2</sup>*Department of Electrical and Computer Engineering, University of Wyoming, Laramie, WY, 82071*

<sup>3</sup>*Material Sciences Center, National Renewable Energy Laboratory, Golden, Colorado 80401*

<sup>4</sup>*Materials Science and Engineering Division, National Institute of Standards and Technology, Gaithersburg, Maryland 20899*

(Dated: 13 December 2020)

Preparation techniques for producing films of individualized solution-dispersed nanoparticles (NPs) for optical spectroscopy are often technically challenging and tailored for a specific NP system. In this work, we present a rapid, easy, and economical technique for producing polyvinyl acetate (PVAc)-based NP-polymer films on the order of 100's of microns thick that exhibit high uniformity, low aggregation, excellent optical transparency, and low terahertz absorption. In addition, we find that these films are robust at cryogenic temperatures and have a high laser damage threshold of  $0.3 \text{ TW cm}^{-2}$ , which make them suitable for pulsed laser measurements. We show that free-standing, flexible, PVAc films can incorporate both one-dimensional single-wall carbon nanotubes (SWCNTs) and zero-dimensional Au NPs. Using absorbance, Raman scattering, and photoluminescence excitation spectroscopy, we observe that SWCNT individualization is maintained, and minimized polymer strain imposed, when the nanotubes are transitioned from solution to the polymer host. This PVAc-based polymer host presents researchers with a straightforward method for producing free-standing and flexible NP films with low aggregation.

## I. INTRODUCTION

A wide variety of nanoparticle (NP) systems, ranging from colloidal nanocrystals to single-wall carbon nanotubes (SWCNTs) to nanoplatelets, are synthesized using solvent-based techniques. Although solutions (aqueous, inorganic, or organic) are usually the preferred environments for these nanomaterials, researchers often require their NPs to be in a solid form for additional measurements, integration into a device or apparatus, and/or technological implementation. When NPs are intentionally transitioned from the solution state to a solidified form, say, for example, for spectroscopic measurements, certain key considerations are required. For optical spectroscopy in particular, the NP host or substrate must show some degree of transparency, stability over a reasonable time duration, and resistance to damage from experimental conditions (light, temperature, magnetic field, etc.). These conditions can often be fairly easily met with the appropriate forethought and material selection process. However, additional requirements are often needed beyond these bare-minimum constraints. When the NP host goes from a solution environment to a gel or solid, the properties of the NPs are often altered due to factors such as NP aggregation<sup>1</sup>, host-created strain<sup>2</sup>, unwanted environmental coupling, and increased optical scattering<sup>3</sup>. These unwanted behaviors add another, more stringent, level of host-material constraints, especially since the desired NP properties are often masked by these effects.

Given the premium that researchers and technical facilitators have placed on using NPs in a solid-state form, numerous techniques to incorporate solution-based NPs into films, solids, and/or solid-state inclusions have proliferated. In addition to simple drop casting and ink printing<sup>4,5</sup>, researchers use transmembrane vacuum filtration<sup>6–11</sup>, inclusion

into hydrogels<sup>12</sup>, polymer-exchange processes<sup>13</sup>, dry pressing<sup>14</sup>, spin coating solutions across substrates<sup>15,16</sup>, shearing NPs between substrates<sup>17</sup>, dip<sup>18</sup> and spray coating<sup>19–22</sup>, and deposition or synthesis in a polymer matrix<sup>23–35</sup>. Many of these techniques require multiple processing steps, considerable time, specialized equipment, and an assortment of chemicals, which makes them very challenging to implement and use by non-specialists. Additionally, the use of dry pressing, spin/dip/spray coating, and inclusion into different hydrogel or polymer matrix hosts often adds a significant amount of NP aggregation and/or strain<sup>1,23,36</sup>. Furthermore, it is often the case that the best non-NP host/substrate medium is not ideal for particular optical regimes, such as the low-energy (long-wavelength) spectrum, where transparencies in the mid-infrared ( $\approx 5 \mu\text{m}$  to  $20 \mu\text{m}$ ) and/or far-infrared/terahertz (THz) ( $30 \mu\text{m}$  to  $3000 \mu\text{m}$  or  $10 \text{ THz}$  to  $0.1 \text{ THz}$ ) regions are required.

In this work, we present a rapid, facile, low-cost method for producing free-standing, flexible, and robust polyvinyl acetate- (PVAc-) based films that have low absorption in both optical and THz regimes. Using a combination of empirical and machine-learning techniques, we find the optimal drying conditions to reliably produce optical-quality samples. Additionally, we show that one- and zero-dimensional aqueous-based NPs can be included into these polymer matrices without significant NP aggregation or changes in their optical response. Specifically, we demonstrate that minimal strain is created in SWCNTs and Au NPs when immersed in these PVAc-based films. Taken together, we reveal a straightforward method for optical spectroscopists to create high-quality, low scatter films for measurements that cover a broad electromagnetic spectrum.

## II. MATERIALS AND METHODS

The base polymer matrix for these films is a commercially available PVAc-based polymer solution (Clear Elmer's Glue™)<sup>37</sup>. Aliquots of this solution were either drop cast onto glass coverslips or spincoat (Laurell WS-400B-GNPP/LITE) at 100 rpm ( $10.5 \text{ rad s}^{-1}$ ) for 40 minutes under controlled air flow and temperature,  $T$ . As discussed later, we used a variety of air flow rates, temperatures, NP mass loading, and drying times to produce optical-quality polymer films. Typically, the highest film uniformity was achieved using a spincoater, but drop casting also created excellent films. Once dried, polymer samples were peeled off of the coverslip with a razorblade and used as free-standing structures, a process illustrated in Figure 1a.

To create NP-immersed PVAc films, we vortexed mixtures of 60% NP solution and 40% PVAc solution (by mass fraction) together in 1.5 mL centrifuge tubes. In addition to this optimized 60:40 NP-to-PVAc solution ratio, we also found other ratios near this split could also produce high-quality films.

Unsorted SWCNTs produced using the CoMoCat process were purchased as raw powder from Sigma Aldrich (Carbon Nanotube, single-walled, (6,5) chirality, batch number: MKBS9733V); this soot is commonly described as SG65i material. Sorted SWCNTs were enriched from a different CoMoCat process source soot obtained directly from Southwest Nanotechnologies (batch number: SG76-L24). SWCNT powders were tip sonicated (Branson Sonifier 250) using a  $\frac{1}{4}$ " (6.35 mm) microtip at  $10 \text{ W mL}^{-1}$  nominal input power for 4.5 hours ( $0.145 \text{ W mL}^{-1}$  to  $0.19 \text{ W mL}^{-1}$  transferred) for 10 mL to 15 mL of  $1 \text{ mg mL}^{-1}$  SWCNTs in 2% DOC<sup>38</sup>. From these solutions, enriched SWCNTs were made using aqueous two-phase extraction (ATPE)<sup>39-42</sup>. Along with the preparation of individualized SWCNT solutions for our immersed NPs, we also used citrate-capped 40 nm diameter Au NPs in an aqueous solution, which were purchased from Nanocomposix.

Several spectroscopic techniques were used in this work, including optical absorption (Varian Cary 500 Scan spectrophotometer), Fourier-transform infrared spectroscopy (FTIR) (Bruker Tensor 27), THz time-domain spectroscopy (TTDS), Raman spectroscopy, and photoluminescence excitation spectroscopy (PLE), which were all performed on polymer films with and without NPs. To ascertain the pulsed laser-induced damage threshold (LIDT) of the PVAc-based polymer film, we focused an amplified, 4 mJ/pulse,  $\approx 200$  fs, 800 nm Ti:S laser (Libra from Coherent) down to a measured beam waist of  $260 \mu\text{m}$ . For the continuous wave (CW) LIDT measurements, a 3.4 W, 4 MHz linewidth, tunable-wavelength Ti:S laser system (Matisse from Spectra-Physics) set at 765 nm was focused to a measured beam waist of  $264 \mu\text{m}$ .

In addition to experimental observations, we used numerical modeling to understand the role of index of refraction on our Au NP spectra. Specifically, the Au NP plasmonic absorption peaks were compared to a Mie scattering model using the PyMieScatt Python library. For this calculation,

we assumed that all of the gold spheres were the same size. Mie scattering efficiencies were calculated from 450 nm to 659 nm using a wavelength-dependent complex index of refraction for Au<sup>43</sup>.

## III. RESULTS AND DISCUSSION

### A. Optical Characterization of the PVAc-Based Film

We note at the outset that PVAc is a polymer that has been previously used in thin-film spectroscopy, though, its optical properties have not been as comprehensively measured as in this work<sup>32-34</sup>. Many of these PVAc environments have been rendered transparent through the addition of benzene and other processing steps<sup>32,34</sup>. Another polymer material commonly used for optical and THz spectroscopy is polyvinyl alcohol (PVA). Similar to the previously mentioned benzene processing of PVAc, PVA films are frequently made with extensive processing steps that our technique does not require<sup>28-31</sup> making our system much more amenable for quick and effective film preparation. Finally, in addition to this work, other researchers have also used off-the-shelf commercially transparent PVAc-based glues due to their optimized durability, drying properties, and transparencies, as well as their ease of use<sup>33</sup>.

Given that we are evaluating a polymer matrix for multiple types of optical spectroscopy, we examined several standard methods of probing NPs. A prime example is Raman scattering spectroscopy in which the frequency difference between incident and scattered light is measured to provide insights to phonon energies. In Figure 1b, we show the Raman spectrum for the PVAc-only dried polymer film. A distinct feature around  $2900 \text{ cm}^{-1}$ , which we attribute to C-H bonds, is observed. Importantly, the negligibly small magnitude of the polymer Raman spectrum does not interfere with the much larger NP Raman signatures.

We also investigate the applicability of our PVAc films for transmission-based optical measurements. In Figure 1c, we present the optical absorptivity spectrum,  $\alpha(\lambda)$ , of the PVAc-only film from  $0.2 \mu\text{m}$  to  $5000 \mu\text{m}$ . Using a combination of optical absorption, FTIR spectroscopy, and TTDS, we can see that two broad regions of high transparency are clearly discernible. The first region, from  $\approx 300 \text{ nm}$  to  $2800 \text{ nm}$ , shows a low  $\alpha$  below  $5 \text{ mm}^{-1}$ . This key regime extends from the UV through the near-infrared, which makes these polymer matrices especially applicable for biological and medical samples, as well as condensed matter NPs that have important properties in the visible or near-infrared regimes. After that, we observe strong absorption peaks between  $2.5 \mu\text{m}$  and  $27 \mu\text{m}$ , which are consistent with bond-stretching peaks determined in PVAc by Ahmed<sup>44</sup>.

The second region of transparency is one that is very often ignored, especially for aqueous-based materials. From  $\approx 124 \mu\text{m}$  to  $5000 \mu\text{m}$ , we find that the polymer absorptivity is only  $\approx 5 \text{ mm}^{-1}$ . While this absorptivity magnitude is not as low as polymers like polytetrafluoroethylene (PTFE);

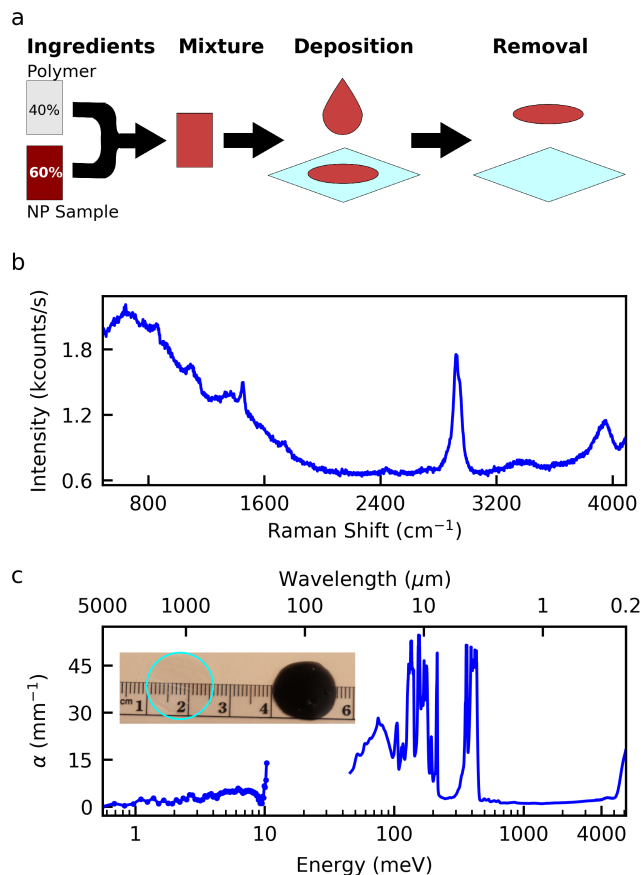


FIG. 1. (a) Films created from a 40% polymer and 60% solution are either drop cast or spin coat onto a glass coverslip. After deposition on the coverslips, these films are left to dry under controlled temperature and air flow conditions before being peeled off the coverslips. (b) Raman spectrum of the PVAc-based polymer film showing the C–H bond stretching peak at  $\approx 2900 \text{ cm}^{-1}$ , along with C–C and C=C bond stretching features near  $\approx 800 \text{ cm}^{-1}$  and  $\approx 1600 \text{ cm}^{-1}$ , respectively. Compared to Raman peaks from NPs, such as nanotubes, these features are insignificant. (c) Optical absorptivity features of the polymer film ranging from the ultraviolet to the THz regime measured via a combination of optical absorption, FTIR, and THz spectroscopy. A small gap in the absorptivity spectrum is present due to the lack of an available spectroscopic source. Flat regions of low absorptivity are observed in the visible and THz regimes, whereas in the mid-infrared region, absorption features due to bond stretching are present<sup>44</sup>.

Teflon), high-density polyethylene (HDPE), and polypropylene, which are roughly an order of magnitude lower, it is comparable to polyacrylonitrile-butadiene-styrene (ABS) and polyethylene terephthalate (PET)<sup>45</sup>. With the increasing use of TTDS for low-energy spectroscopy of condensed matter NPs and bio-medical systems<sup>46,47</sup>, having a matrix that is transparent in this region is critical. Moreover, having a NP host system that is optically transparent in *both* the optical and THz regimes allows for the study of optically created effects

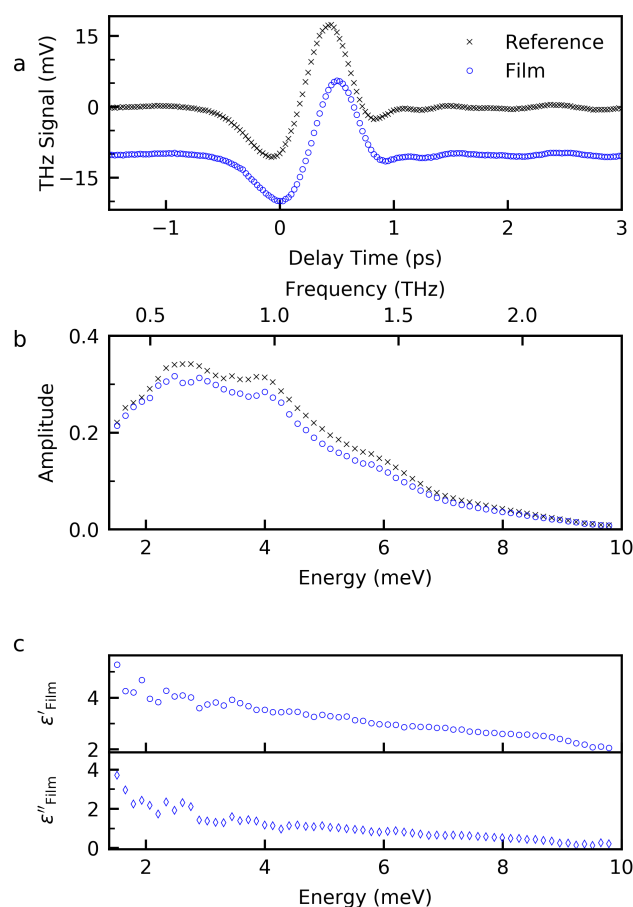


FIG. 2. (a) THz time-domain spectroscopy (TTDS) data for the air reference (black exes) and polymer film without NPs (blue circles). (b) The FFT amplitude for the corresponding TTDS traces. (c) Real ( $\epsilon'_{\text{film}}$ , top) and imaginary ( $\epsilon''_{\text{film}}$ , bottom) calculated relative permittivity for the polymer film as a function of frequency.

that can be probed as a function of time (and frequency) using TTDS as the system returns to equilibrium<sup>48–51</sup>. Though techniques needing both optical and far-infrared wavelengths are not in abundant use, several advanced methods do require such material constraints. Select crystals, such as z-cut quartz, have dual optical and far-infrared transparency windows, but are not amenable to hosting NPs, except when deposited on the surface. Beyond that, very few other materials that can host NPs satisfy this criteria. As such, having this aqueous polymer matrix represents an important advance for hosting NPs relevant to visible, near-infrared, and far-infrared spectroscopists.

As already discussed, the low and flat absorptive region that begins around  $125 \mu\text{m}$  and continues to  $5000 \mu\text{m}$  (the extent of our TTDS bandwidth) represents a significant area of THz transparency, which is surprising in a polymer due to molecular rotational and vibrational modes. Figure 2(a) shows the TTDS time traces for the air reference and PVAc polymer film. Since we are measuring the actual THz electric field with this technique, a transformation into the fre-

quency domain [Figure 2(b)] allows us to calculate the real and imaginary parts of the electric permittivity,  $\epsilon'_{\text{film}}$  and  $\epsilon''_{\text{film}}$ , respectively, for the PVAc-based polymer. Figure 2(c) shows  $\epsilon'_{\text{film}}$  and  $\epsilon''_{\text{film}}$  for our films from 200 GHz to 2.5 THz. Although  $\epsilon'_{\text{film}}$  is close in value to other polymers, such as PET, polyaramid, polymethylmethacrylate (PMMA), and HDPE, it varies from 4 to 2 within a short frequency range. As a comparison, across a similar region, PET varies from 3.0 to 2.7<sup>45</sup>. Similarly, we see a high degree of variability in  $\epsilon''_{\text{film}}$ , although this value is much more in line with other transparent polymers. We suspect that inconsistencies in the thickness across the film (higher at the edges and lower in the middle) may account for some of the variability. Unlike other optical measurements, the beam spot sizes in TTDS vary strongly with frequency due to the order of magnitude span of wavelengths in the far-infrared covered by the pulse. If smaller frequencies probe, on average, thicker regions of the polymer film while larger frequencies measure thinner regions, then this effect could help account for the steep negative slope of both  $\epsilon'_{\text{film}}$  and  $\epsilon''_{\text{film}}$ . However, that still would not change the overall conclusions shown in the figure, but rather, would suggest that the true value of  $\epsilon'_{\text{film}}$  and  $\epsilon''_{\text{film}}$  for the probed spectral regime lies around 5 meV to 6 meV ( $\approx 1.2$  THz to 1.5 THz).

## B. Film Quality Categorization

Given these encouraging optical results, we next investigated the environmental conditions necessary to reproducibly make high-quality films. Depending on the drying parameters used, the structure of the dried PVAc-based films varied considerably. To qualitatively categorize our films for use in spectroscopic measurements, we defined a 1 cm diameter region of interest (ROI) at the center of the film. Either SWCNT NPs or green dye was included into the polymer films to clearly indicate regions of inhomogeneity and particulate clumping. Three assessment categories were defined for determining the suitability of a given film for spectroscopic work: ‘highest optical quality’, ‘high optical quality’, and ‘low optical quality’. We defined a ‘highest optical quality’ film as one that has a highly homogenous NP dispersion that is also free of any defects. Here, we define defects as bubbles, differential tension drying rings, thickness variations, and visible sample concentration variations. When a film was considered to be ‘high optical quality’, the ROI was free of defects, but they existed elsewhere in the film. If defects were located in the ROI or if they were spaced such that a 1 cm diameter defect-free region could not be located in the sample, the film was considered ‘low optical quality’; for this latter result, the films are not suitable for use in optical experiments.

We explored NP loading (fraction of the film composed of NPs), polymer-to-solution ratios, spin-coating speed, spin-coating duration, film diameter, temperature, and applied drying air flow to determine the conditions that produced PVAc-based films devoid of defects. Several of these parameters, such as NP loading and the polymer-to-solution ratios, were quickly established and were consequently held fixed, while others we changed to optimize. Figure 3 shows a plot of qual-

itative description of films as a function of temperature, air flow, and post-dropcast or -spin-coat drying duration. Films that either had a 25 mm or 50 mm diameter were included in this assessment.

To aid with understanding this drying parameter space, we use a machine-learning algorithm to predict values of temperature, applied air flow, and drying duration that would likely result in, at minimum, ‘high optical quality’ films. Our machine-learning algorithm is based on a k-nearest neighbors (KNN) algorithm was applied to the given data set. As a classification learning algorithm, where predictions are based on the statistical assumption that similar outcomes lie within a given distance (Euclidean) away from each other, KNN lends itself nicely to the given parameter space and classifiers. After a trained model was created based on the given data set, we fed permutations of different parameters into the model and extracted predictions of a ‘high optical quality’ film.

Along with actual data points, Figure 3 shows (in green) the KNN-predicted parameter space where ‘high optical quality’ films can be produced. These regions, which like the actual data points are projected along 2D planes, help provide strong drying parameter estimates for other researchers using our film-making procedure. Probably the most significant prediction is that somewhat high (25° C to 75° C) temperatures coupled with a strong ( $\approx 25$  mL/s to 35 mL/s) air flow are expected to yield the best drying conditions. A reasonable place to start experiments, however, would be 40° C and  $\approx 25$  mL/s. Although we have found empirically several high quality films outside of this sweet spot, as well as several low quality films inside of it, we maintain that by and large, the best set of drying parameters is in this range. We note that defects are often formed when one or more small bubbles make their way into the film as it dries. The qualitative nature of our assessment means that the placement and number of these small bubbles can easily change our film description. Thus, a region of drying parameters that is most likely to produce ‘high optical quality’ films will always produce some ‘low optical quality’ films. This unavoidable spread in bubble placement, however, does not undermine our confidence in claiming that our method is reproducible.

## C. Optical Damage Threshold and Cryogenic Freezing Experiments

A key condition for using any type of host for pulsed optical spectroscopy is the ability to withstand high intensities (power per unit area) and fluence (energy per unit pulse per unit area). The use of polymers in pulsed laser experiments have traditionally been avoided due to the the low thermal conductivities, heat capacities, and structure damage thresholds of polymers relative to hard condensed matter systems. To assess the suitability of our PVAc-based polymer for intense field work, we performed laser-induced damage threshold (LIDT) measurements with pulsed and CW lasers.

To assess the pulsed LIDT of our polymer films, we used a 200 fs amplified pulsed laser with a central wavelength of 800 nm and a repetition rate of 1 kHz. For these LIDT measure-

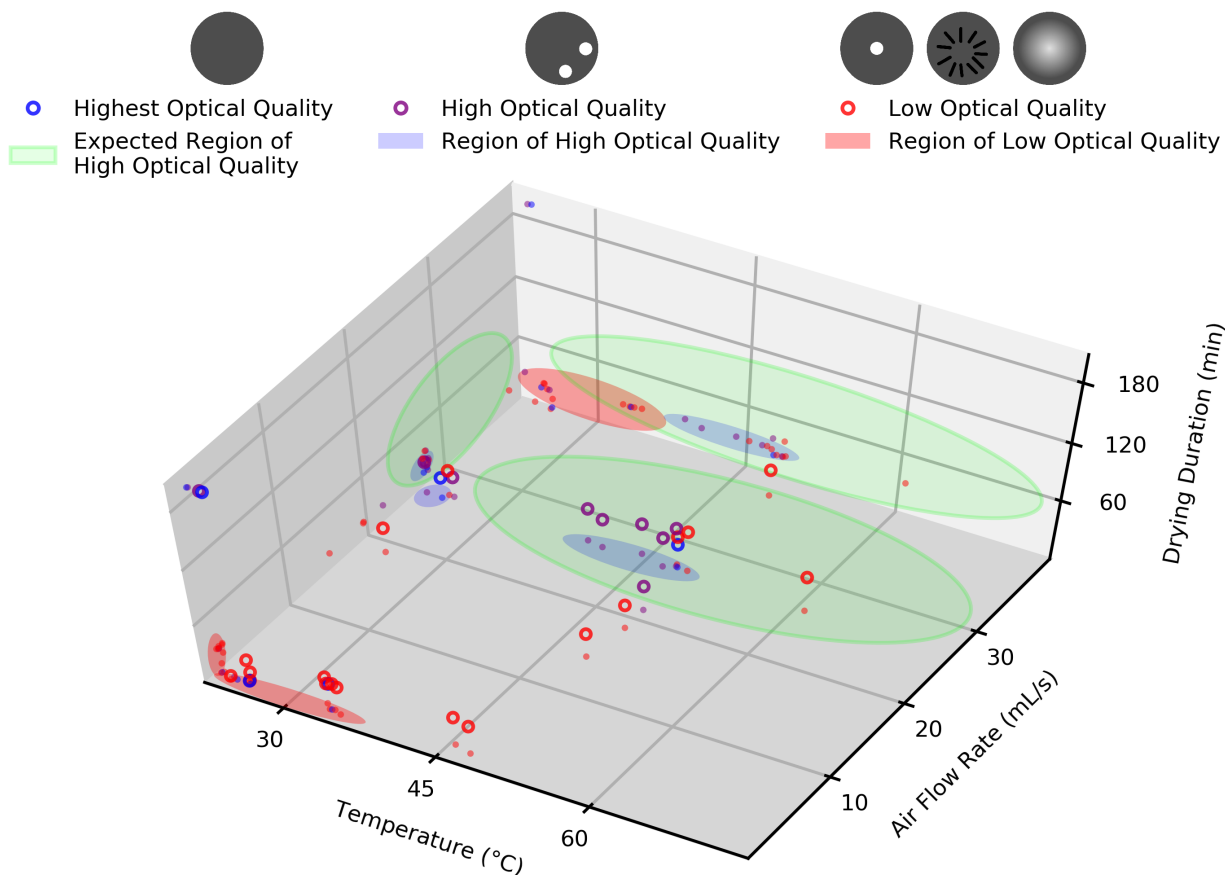


FIG. 3. Map of the film casting parameter space with each film qualitatively categorized by the presence of defects within a 1 cm-diameter region of interest (ROI). ‘Highest optical quality’ films have no visible defects across the entire film and are the best achievable outcome possible on our qualitative scale. ‘High optical quality’ films contained no defects within the ROI, which allows for their use in a wide range of optical experiments. ‘Low optical quality’ polymer films had defects within the ROI and were considered unsuitable for spectroscopic work. In addition to plotting these qualitative film assessments onto a three-axis parameter space, we show these results as two-dimensional projections. Also plotted here (green shading) are regions in this parameter space that we predict, via a machine-learning algorithm, good drying parameters for creating, at minimum, ‘high optical quality’ films.

ments and the ones using a CW laser, we measured the power of the transmitted light both with and without the polymer film. The pulsed LIDT measurements on our polymer films revealed that at a peak intensity  $0.29 \text{ TW cm}^{-2}$ , we began to observe damage to the polymer. In contrast, the CW LIDT experiment showed that damage occurred at an average intensity of  $2.2 \text{ TW cm}^{-2}$ . However, we note that this LIDT value is an averaged quantity due to spatial variations created by microscopic inhomogeneities in the film. To put these values for this PVAc-based polymer into context, the CW LIDT for Ge is  $\approx 0.3 \text{ MW cm}^{-2}$ <sup>252</sup>, while modern femtosecond beamline mirrors have a pulsed LIDT of  $2.5 \text{ TW cm}^{-2}$ <sup>253</sup>. Our LIDT values are comparable to these systems only because the absorptivity of our films for the UV-visible-IR region is so low: by absorbing very little light, the process of optically induced thermal strain leading to material damage is greatly reduced.

In addition to the LIDT experiments, we also immersed these films into liquid nitrogen, and separately, brought them down to 5 K. In both cases, due to the negligible water remaining in the films after drying, these polymers (both with

and without NPs) showed that they could survive cryogenic freeze-thaw cycling without any structural damage. Unlike aqueous-based polymeric hosts and certain crystals, these PVAc-based polymer films can be used for low temperature work.

#### D. SWCNT Nanoparticle Polymer Films

We created SWCNT-polymer films to determine the ability of this polymer system to host 1D NPs without significant aggregation or induced strain; an example of a SWCNT-polymer film is shown in the inset of Figure 1c. To measure the local environment of SWCNTs, we relied on optical measurements of their vibration properties, absorption features, and emission characteristics, which are well known to be excellent determinants of strain, aggregation (bundling), and optical/electronic proximity.

Figure 4a shows the Raman spectra from both the SWCNT starting solution and SWCNTs from that solution in a dried

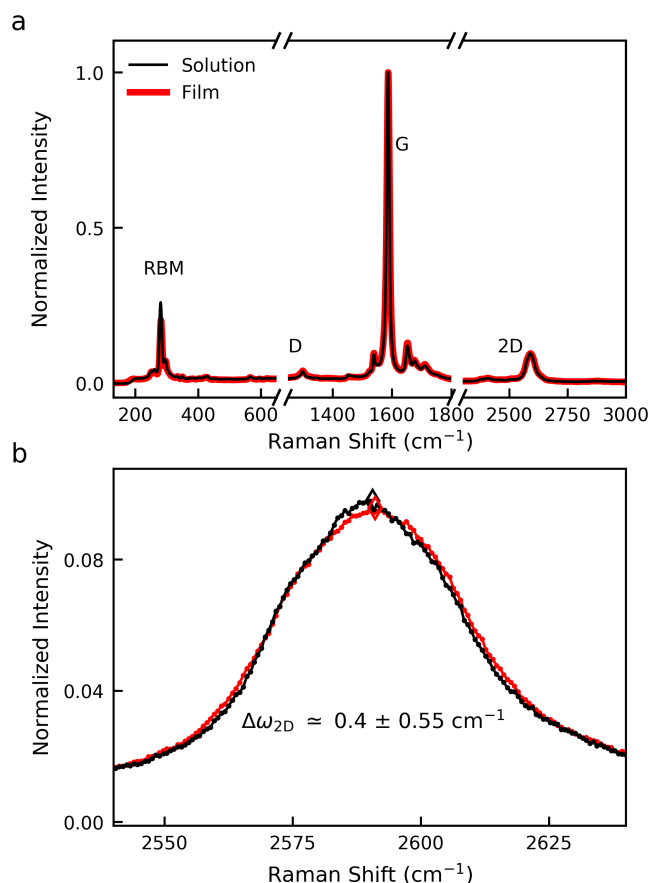


FIG. 4. (a) Raman spectra of unsorted SWCNTs in solution (black) demonstrating the same peaks associated with SWCNTs occur in both the solution and the film consisting of the radial-breathing modes (RBM), G, D, and 2D Raman features. While the C–H bond stretching peak due to the polymer matrix is present, it is barely visible at this scale. (b) We use Gaussian fitting of the 2D peak to determine the very small shift due to strain on the SWCNTs. From our calculations, we estimate a difference of  $\approx 0.4 \text{ cm}^{-1} \pm 0.5 \text{ cm}^{-1}$ , which corresponds to a strain of  $\approx 0.03\% \pm 0.03\%$ <sup>54</sup>. Here, error is defined as the Gaussian width of the spectral fits.

PVAc-based polymer film. Importantly, all of the Raman spectroscopic signatures of the SWCNTs, including the radial-breathing mode (RBM), G and D peaks, and 2D peak<sup>55–57</sup>, are clearly maintained when the SWCNT solution is incorporated into the polymer host. To determine if the incorporated SWCNTs are subjected to any polymer-induced strain, we compared the 2D Raman feature from SWCNTs in solution to those in the film. As seen in Figure 4b, the shift between these two SWCNT environment conditions is barely visible. From the change in the Raman 2D peak position between film and solution environments of  $\approx 0.4 \text{ cm}^{-1} \pm 0.5 \text{ cm}^{-1}$ , we estimate a possible polymer-induced strain on SWCNTs of  $\approx 0.03\% \pm 0.03\%$  from known relationships between Raman shifts and strain<sup>54</sup>. We note for clarity that we are defining error here as the Gaussian width obtained from our spectral fitting. While this strain value is

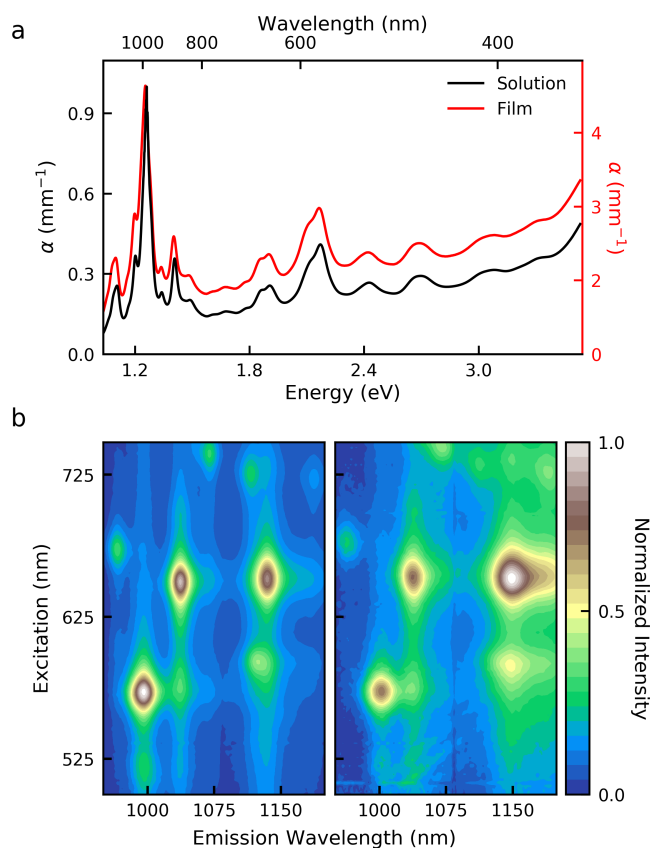


FIG. 5. (a) Optical absorption of unsorted SWCNTs, which is defined by sharply peaked exciton absorption features, for SWCNTs in solution (black) and after they have been incorporated into polymer films (red). The SWCNTs in the polymer host maintain highly defined absorption features and exhibit only small spectral shifts in their absorption spectrum, which both indicate only a small effect of the polymer host on the incorporated SWCNT NPs. (b) Photoluminescence excitation (PLE) maps of the sorted semiconductor-enriched SWCNTs in solution (left) and SWCNT-polymer film (right). The small degree of bundling is indicated through the clear presence of SWCNT chiralities, as shown via unique excitation and emission combinations. Inter-chirality contributions, seen through the presence of emission occurring between high intensity peaks, suggest a small amount of bundling created through incorporation into the polymer host. Each map is normalized to the highest PLE feature in the data set.

low compared to other strain measurements on SWCNTs, the uncertainty of the small change in the peak position is comparable (if not larger) than the actual change, suggesting that within our ability to measure, the strain-induced peak shift is insignificant.

Absorption peaks in the visible to near infrared region, shown in Figure 5a, correspond to exciton (optically created, Coulombically bound electron-hole pairs) absorption features in SWCNTs. Given their relationship to both the SWCNT band structure and the nanotube dielectric environment, the position and linewidth of these absorption features are sensitive to the immediate environment of the SWCNTs<sup>20,58–62</sup>.

Although all of the absorption features observed in the parent solution are indeed preserved in the film with minimal broadening and minor peak shifts, our best confirmation of SWCNT individualization (*i.e.*, minimized aggregation) is through PLE. For SWCNT chirality identification, researchers use the unique combination of an excited exciton absorptive transition (typically done at optical frequencies) and emissive transition (usually measured in the near-infrared)<sup>55–57</sup>. A SWCNT excitation that produces multiple emissions, instead of a single one, corresponds to either a closely associated chirality, a phonon-assisted transition, or an energetic coupling between different chiralities that is indicative of aggregation (bundling)<sup>13</sup>.

Figure 5b compares PLE measurements of sorted semi-conducting SWCNTs in solution and in a PVAc-based film. The transition of the solution-state SWCNTs to a film-based solid shows minimal additional emissions from different coupled SWCNTs. The small degree of increased inter-chirality SWCNT coupling suggests that although nanotube bundling has increased in the PVAc-based film, it is still relatively minimal compared to previous SWCNT film examples<sup>6,7,9–11,28,29,63,64</sup>.

### E. Gold Nanoparticle Polymer Films

To extend the applicability of these PVAc-based films, we examined including citrate-capped Au NPs into this polymer host while still preserving their most important optical properties. Based on the specified NP diameter of 40 nm, we expected a plasmonic scattering peak at 524 nm from estimates via Mie scattering calculations of Au NPs surrounded by water ( $n = 1.33$ ). This estimate is very close to the measured plasmonic peak in solution of 522 nm, as seen in Figure 6. After incorporating these NPs into a PVAc-based film, the NP scattering peak shifted by 16 nm ( $\approx 70$  meV) to 540 nm. In addition to the peak position shift, the Gaussian width was broadened from 21 nm to 29 nm.

As before, the shift in the scattering peak value to a higher wavelength is in excellent agreement with Mie scattering predictions: we used exactly the same NP parameters as for the solution case, except now, we have changed the surrounding index of refraction to 1.484 to account for the polymer host. Plasmonic scattering features from individualized NPs are known to be dependent on the indices of refraction of both the particles themselves, as well as the surrounding medium<sup>65</sup>, which means that this matching of experimental and computational results through an index of refraction substitution provides three key pieces of information: first, a confirmation that the majority of the observed peak shift is due to NP medium optical effects; second, an implicit confirmation of the continued individualization of the Au NPs even in a polymer host; and third, an estimate of the index of refraction for our PVAc-based polymer in this wavelength regime. The agreement between our experimental observations and model calculations shown in Figure 6 strongly suggests that the change in the index of refraction of the surrounding medium (water to PVAc) is responsible for the scattering peak shift.

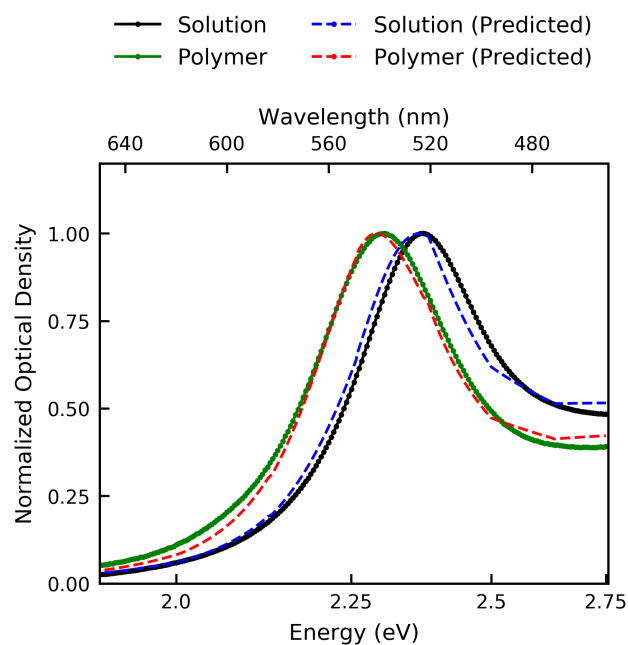


FIG. 6. Normalized plasmonic scattering from Au NPs from experimental and computational sources. The computed scattering curves are calculated using Mie scattering functions, where the only difference in the two calculated curves is a change in the index of refraction of the surrounding medium. The experimental and computational curves for Au NPs in solution and film are in excellent agreement with one another and suggest polymer-created strain effects are minimal here.

This conclusion does not imply that polymer-created strain is not present, but rather, it is a minimal effect on the optical properties of these NPs, similar to our observations with SWCNTs. We note that more direct methods for measuring and understanding NP agglomeration than we used here, such as small-angle scattering methods (e.g., small-angle neutron scattering, dynamic light scattering, and small-angle x-ray scattering)<sup>66</sup> and electron microscopy (e.g., multiple thin slices imaged by transmission electron microscopy), are available. However, while these methods measure the inter-nanoparticle spacing and NP aggregate size distribution and average density, they are highly complex and challenging to correctly use, which suggests the need for further work on this PVAc-based polymer.

### F. Compatibility with Different Solvents

In addition to water, we also tried to create polymer films using both polar (methanol, ethanol, and acetonitrile) and non-polar solvents (hexanes, toluene, and chloroform). As with the films made with water, each solvent was mixed and vortexed with the PVAc-based polymer as described earlier. At this juncture, separation was observed when hexanes and toluene were used, while chloroform, methanol, and acetonitrile created an opaque, congealed mass. Only films

made with ethanol produced transparent, stable films, albeit never comparable in quality to those made with water.

#### IV. CONCLUSIONS

We used a commercial PVAc-based polymer to create thin, transparent films that could host NPs of different dimensionality, specifically SWCNTs and Au NPs, without significant aggregation. Based off our spectroscopic findings and the fact that we believe that the polymer agglomeration mechanism in this system is not strongly based on the NP electronic properties, it is likely that this polymer matrix can also be used for semiconducting and insulating (e.g., nitride and oxide) NPs. In addition to studying polymer-created aggregation, we also showed that the complex permittivity from 0.2 THz to 2.5 THz is similar to other polymers. Unlike other NP polymer hosts, this PVAc system can be easily cast with and without NPs into large (2.5 cm to 5.0 cm) films with high transparency in both the optical and THz regimes. Our work enables other researchers to quickly and efficiently produce high-quality NP polymer films for optical spectroscopic work in a variety of environments.

#### ACKNOWLEDGMENTS

H. V. Wladkowski and W. D. Rice thank the University of Wyoming School of Energy Resources for support. This work was authored by the National Renewable Energy Laboratory, operated by Alliance for Sustainable Energy, LLC, for the U.S. Department of Energy (DOE) under Contract No. DE-AC36-08GO28308. Funding for J. L. Blackburn provided by the U.S. DOE, Office of Science, Office of Basic Energy Sciences, Division of Chemical Sciences, Geosciences, and Biosciences, Solar Photochemistry Program. The views expressed in the article do not necessarily represent the views of the DOE or the U.S. Government. J. A. Fagan was supported by National Institute of Standards and Technology internal funds.

#### DATA AVAILABILITY

The data that support the findings of this study are available from the corresponding author upon reasonable request.

#### REFERENCES

- <sup>1</sup>A.-C. Genix, V. Bocharova, B. Carroll, M. Lehmann, T. Saito, S. Krueger, L. He, P. Dieudonné-George, A. P. Sokolov, and J. Oberdisse, "Understanding the static interfacial polymer layer by exploring the dispersion states of nanocomposites," *ACS Appl. Mater. & Inter.* **11**, 17863 (2019).
- <sup>2</sup>Y. Li, K. Wang, and Z. Su, "Dispersed sensing networks in nano-engineered polymer composites: From static strain measurement to ultrasonic wave acquisition," *Sensors* **18**, 1398 (2018).

- <sup>3</sup>T. Erdem, L. Yang, P. Xu, Y. Altintas, T. O'Neil, A. Caciagli, C. Ducati, E. Mutlugun, O. A. Scherman, and E. Eiser, "Transparent films made of highly scattering particles," *Langmuir* **36**, 911–918 (2020).
- <sup>4</sup>U. Khan, P. May, H. Porwal, K. Nawaz, and J. N. Coleman, "Improved Adhesive Strength and Toughness of Polyvinyl Acetate Glue on Addition of Small Quantities of Graphene," *ACS Applied Materials & Interfaces* **5**, 1423–1428 (2013).
- <sup>5</sup>S. J. Kim, H. Wu, D.-I. Moon, M.-L. Seol, B. Kim, D. I. Lee, J.-W. Han, and M. Meyyappan, "Carbon Nanotube Based  $\gamma$  Ray Detector," *ACS Sensors* **4**, 1097–1102 (2019).
- <sup>6</sup>Z. Wu, Z. Chen, X. Du, J. M. Logan, J. Sippel, M. Nikolou, K. Kamaras, J. R. Reynolds, D. B. Tanner, A. F. Hebard, and A. G. Rinzler, "Transparent, Conductive Carbon Nanotube Films," *Science* **305**, 1273–1276 (2004).
- <sup>7</sup>Y. Zhou, L. Hu, and G. Grüner, "A method of printing carbon nanotube thin films," *Appl. Phys. Lett.* **88**, 123109 (2006).
- <sup>8</sup>Y. Liu, M. Nitschke, L. Stepien, V. Khavrus, V. Bezugly, and G. Cuniberti, "Ammonia Plasma-Induced n-Type Doping of Semiconducting Carbon Nanotube Films: Thermoelectric Properties and Ambient Effects," *ACS Appl. Mater. & Inter.* **11**, 21807–21814 (2019).
- <sup>9</sup>A. A. Green and M. C. Hersam, "Colored Semitransparent Conductive Coatings Consisting of Monodisperse Metallic Single-Walled Carbon Nanotubes," *Nano Lett.* **8**, 1417–1422 (2008).
- <sup>10</sup>X. He, W. Gao, L. Xie, B. Li, Q. Zhang, S. Lei, J. M. Robinson, E. H. Hároz, S. K. Doorn, W. Wang, R. Vajtai, P. M. Ajayan, W. W. Adams, R. H. Hauge, and J. Kono, "Wafer-scale monodomain films of spontaneously aligned single-walled carbon nanotubes," *Nature Nanotechnol.* **11**, 633–638 (2016).
- <sup>11</sup>J. S. Walker, J. A. Fagan, A. J. Biacchi, V. A. Kuehl, T. A. Searles, A. R. H. Walker, and W. D. Rice, "Global Alignment of Solution-Based Single-Wall Carbon Nanotube Films via Machine-Vision Controlled Filtration," *Nano Lett.* **19**, 7256–7264 (2019).
- <sup>12</sup>E. P. Gilshteyn, S. Lin, V. A. Kondrashov, D. S. Kopylova, A. P. Tsapenko, A. S. Anisimov, A. J. Hart, X. Zhao, and A. G. Nasibulin, "A One-Step Method of Hydrogel Modification by Single-Walled Carbon Nanotubes for Highly Stretchable and Transparent Electronics," *ACS Appl. Mater. & Inter.* **10**, 28069–28075 (2018).
- <sup>13</sup>D. H. Arias, D. B. Sulas-Kern, S. M. Hart, H. S. Kang, J. Hao, R. Ihly, J. C. Johnson, J. L. Blackburn, and A. J. Ferguson, "Effect of nanotube coupling on exciton transport in polymer-free monochiral semiconducting carbon nanotube networks," *Nanoscale* **11**, 21196 (2019).
- <sup>14</sup>B.-W. Wang, S. Jiang, Q.-B. Zhu, Y. Sun, J. Luan, P.-X. Hou, S. Qiu, Q.-W. Li, C. Liu, D.-M. Sun, and H.-M. Cheng, "Continuous Fabrication of Meter-Scale Single-Wall Carbon Nanotube Films and their Use in Flexible and Transparent Integrated Circuits," *Adv. Mater.* **30**, 1802057 (2018).
- <sup>15</sup>V. Lahariya, "Study of Electroluminescence in Cadmium Sulfide Polymer Nanocomposite Films," *J. Nano Research* **49**, 181–189 (2017).
- <sup>16</sup>D. Tanaka, N. Aketa, H. Tanaka, S. Horike, M. Fukumori, T. Tamaki, T. Inose, T. Akai, H. Toyama, O. Sakata, H. Tajiri, and T. Ogawa, "Facile preparation of hybrid thin films composed of spin-crossover nanoparticles and carbon nanotubes for electrical memory devices," *Dalton Trans.* **48**, 7074–7079 (2019).
- <sup>17</sup>C. Sui, Z. Pan, R. J. Headrick, Y. Yang, C. Wang, J. Yuan, X. He, M. Pasquali, and J. Lou, "Aligned-SWCNT film laminated nanocomposites: Role of the film on mechanical and electrical properties," *Carbon* **139**, 680–687 (2018).
- <sup>18</sup>B. Gao, X. Zhang, S. Qiu, H. Jin, Q. Song, and Q. Li, "Assembly of aligned semiconducting carbon nanotubes in organic solvents via introducing intertube electrostatic repulsion," *Carbon* **146**, 172–180 (2019).
- <sup>19</sup>D. Shim, S.-H. Jung, S. Y. Han, K. Shin, K.-H. Lee, and J. H. Han, "Improvement of SWCNT transparent conductive films via transition metal doping," *Chem. Comm.* **47**, 5202 (2011).
- <sup>20</sup>F. Loghini, A. Rivadeneyra, M. Becherer, P. Lugli, and M. Bobinger, "A facile and efficient protocol for preparing residual-free single-walled carbon nanotube films for stable sensing applications," *Nanomaterials* **9**, 471 (2019).
- <sup>21</sup>A. Abdellah, A. Abdelhalim, F. Loghini, P. Kohler, Z. Ahmad, G. Scarpa, and P. Lugli, "Flexible Carbon Nanotube Based Gas Sensors Fabricated by Large-Scale Spray Deposition," *IEEE Sensors Journal* **13**, 4014–4021 (2013).

- <sup>22</sup>T. V. Sreekumar, T. Liu, S. Kumar, L. M. Ericson, R. H. Hauge, and R. E. Smalley, "Single-Wall Carbon Nanotube Films," *Chem. Mater.* **15**, 175–178 (2003).
- <sup>23</sup>N. Akima, Y. Iwasa, S. Brown, A. M. Barbour, J. Cao, J. L. Musfeldt, H. Matsui, N. Toyota, M. Shiraishi, H. Shimoda, and O. Zhou, "Strong anisotropy in the far-infrared absorption spectra of stretch-aligned single-walled carbon nanotubes," *Adv. Mater.* **18**, 1166 (2006).
- <sup>24</sup>A. K. Das, A. Mukherjee, K. Baba, R. Hatada, R. Bhowmik, and A. K. Meikap, "Current-Voltage Hysteresis Behavior of PVA-Assisted Functionalized Single-Walled Carbon Nanotube Free-Standing Film," *J. Phys. Chem. C* **122**, 29094–29105 (2018).
- <sup>25</sup>M. Gnanaseelan, Y. Chen, J. Luo, B. Krause, J. Pionteck, P. Pötschke, and H. Qi, "Cellulose-carbon nanotube composite aerogels as novel thermoelectric materials," *Composites Science and Technology* **163**, 133–140 (2018).
- <sup>26</sup>Z. Xu, Y. Zhang, Z. Wang, N. Sun, and H. Li, "Enhancement of Electrical Conductivity by Changing phase Morphology for Composites Consisting of Polylactide and Poly( $\epsilon$ -caprolactone) Filled with Acid-Oxidized Multiwalled Carbon Nanotubes," *ACS Appl. Mater. & Inter.* **3**, 4858–4864 (2011).
- <sup>27</sup>R. Hagenmueller, H. H. Gommans, A. G. Rinzler, J. E. Fischer, and K. I. Winey, "Aligned single-wall carbon nanotubes in composites by melt processing methods," *Chem. Phys. Lett.* **330**, 219–225 (2000).
- <sup>28</sup>D. Polley, A. Ganguly, A. Barman, and R. K. Mitra, "Polarizing effect of aligned nanoparticles in terahertz frequency region," *Optics Lett.* **38**, 2754 (2013).
- <sup>29</sup>D. Polley, A. Barman, and R. K. Mitra, "EMI shielding and conductivity of carbon nanotube-polymer composites at terahertz frequency," *Optics Lett.* **39**, 1541 (2014).
- <sup>30</sup>D. Polley, A. Barman, and R. K. Mitra, "Controllable terahertz conductivity in single walled carbon nanotube/polymer composites," *J. Appl. Phys.* **117**, 023115 (2015).
- <sup>31</sup>J.-P. Yu, S. Chen, F. Fan, S.-T. Xu, J.-R. Cheng, X.-F. Chen, L. Xiao, and S.-J. Chang, "Accelerating terahertz all-optical modulation by hot carriers effects of silver nanorods in PVA film," *AIP Adv.* **9**, 075017 (2019).
- <sup>32</sup>W. E. Mahmoud, A. A. Al-Ghamdi, and F. Al-Agel, "Synthesis and optical properties of poly (vinyl acetate)/bismuth oxide nanorods," *Polymers for Advanced Technologies* **22**, 2055–2061 (2010).
- <sup>33</sup>P. A. Kurian, C. Vijayan, K. Sathiyamoorthy, C. S. S. Sandeep, and R. Philip, "Excitonic Transitions and Off-resonant Optical Limiting in CdS Quantum Dots Stabilized in a Synthetic Glue Matrix," *Nanoscale Research Lett.* **2**, 561–568 (2007).
- <sup>34</sup>M. Abdelaziz, "Optical and dielectric properties of poly(vinylacetate)/lead oxide composites," *J. Mater. Sci.: Mater. in Electronics* **23**, 1378–1386 (2011).
- <sup>35</sup>W. Liu, F. Fan, S. Xu, M. Chen, X. Wang, and S. Chang, "Terahertz wave modulation enhanced by laser processed PVA film on Si substrate," *Sci. Rep.* **8**, 8304 (2018).
- <sup>36</sup>T. S. Soliman and S. A. Vshivkov, "Effect of Fe nanoparticles on the structure and optical properties of polyvinyl alcohol nanocomposite films," *J. of Non-Crystalline Solids* **519**, 119452 (2019).
- <sup>37</sup>"Certain equipment, instruments or materials are identified in this paper in order to adequately specify the experimental details. such identification does not imply recommendation by the national institute of standards and technology (nist) nor does it imply the materials are necessarily the best available for the purpose."
- <sup>38</sup>M. J. O'Connell, S. M. Bachilo, C. B. Huffman, V. C. Moore, M. S. Strano, E. H. Háróz, K. L. Rialon, P. J. Boul, W. H. Noon, C. Kittrell, J. Ma, R. H. Hauge, R. B. Weisman, and R. E. Smalley, "Band Gap Fluorescence from Individual Single-Walled Carbon Nanotubes," *Science* **297**, 593–596 (2002).
- <sup>39</sup>J. A. Fagan, C. Y. Khripin, C. A. S. Batista, J. R. Simpson, E. H. Háróz, A. R. H. Walker, and M. Zheng, "Isolation of Specific Small-Diameter Single-Wall Carbon Nanotube Species via Aqueous Two-Phase Extraction," *Adv. Mater.* **26**, 2800–2804 (2014).
- <sup>40</sup>N. K. Subbaiyan, S. Cambré, A. N. G. Parra-Vasquez, E. H. Háróz, S. K. Doorn, and J. G. Duque, "Role of Surfactants and Salt in Aqueous Two-Phase Separation of Carbon Nanotubes toward Simple Chirality Isolation," *ACS Nano* **8**, 1619–1628 (2014).
- <sup>41</sup>J. A. Fagan, E. H. Háróz, R. Ihly, H. Gui, J. L. Blackburn, J. R. Simpson, S. Lam, A. R. H. Walker, S. K. Doorn, and M. Zheng, "Isolation of >1 nm Diameter Single-Wall Carbon Nanotube Species Using Aqueous Two-Phase Extraction," *ACS Nano* **9**, 5377–5390 (2015).
- <sup>42</sup>H. Gui, J. K. Streit, J. A. Fagan, A. R. H. Walker, C. Zhou, and M. Zheng, "Redox Sorting of Carbon Nanotubes," *Nano Lett.* **15**, 1642–1646 (2015).
- <sup>43</sup>P. B. Johnson and R. W. Christy, "Optical Constants of the Noble Metals," *Phys. Rev. B* **6**, 4370–4379 (1972).
- <sup>44</sup>R. M. Ahmed, "Study on Different Solution-Cast Films of PMMA and PVAc," *International Journal of Polymeric Materials and Polymeric Biomaterials* **57**, 969–978 (2008).
- <sup>45</sup>Y.-S. Jin, G.-J. Kim, and S.-G. Jeon, "Terahertz dielectric properties of polymers," *J. Korean Phys. Soc.* **49**, 513 (2006).
- <sup>46</sup>M. S. Kulya, E. L. Odlyanitskiy, Q. Cassar, I. A. Mustafin, V. N. Trukhin, P. G. Gavrilova, D. V. Korolev, Y. A. Kononova, N. S. Balbekin, P. Mounaix, J.-P. Guillet, N. V. Petrov, and O. A. Smolyanskaya, "Fast terahertz spectroscopic holographic assessment of optical properties of diabetic blood plasma," *J. Infrared, Millimeter, and Terahertz Waves*, 1041–1056 (2020).
- <sup>47</sup>R. Gente, A. Rehn, T. Probst, E.-M. Stübling, E. C. Camus, A. A. Covarrubias, J. C. Balzer, and M. Koch, "Outdoor Measurements of Leaf Water Content Using THz Quasi Time-Domain Spectroscopy," *Journal of Infrared, Millimeter, and Terahertz Waves* **39**, 943–948 (2018).
- <sup>48</sup>S. Kar and A. K. Sood, "Ultrafast terahertz photoresponse of single and double-walled carbon nanotubes: Optical pump-terahertz probe spectroscopy," *Carbon* **144**, 731–736 (2019).
- <sup>49</sup>J. L. Blackburn, T. M. Barnes, M. C. Beard, Y.-H. Kim, R. C. Tenent, T. J. McDonald, B. To, T. J. Coutts, and M. J. Heben, "Transparent Conductive Single-Walled Carbon Nanotube Networks with Precisely Tunable Ratios of Semiconducting and Metallic Nanotubes," *ACS Nano* **2**, 1266–1274 (2008).
- <sup>50</sup>L. Luo, I. Chatzakis, A. Patz, and J. Wang, "Ultrafast Terahertz Probes of Interacting Dark Excitons in Chirality-Specific Semiconducting Single-Walled Carbon Nanotubes," *Phys. Rev. Lett.* **114**, 107402 (2015).
- <sup>51</sup>L. Luo, Z. Liu, X. Yang, C. Vaswani, D. Cheng, J.-M. Park, and J. Wang, "Anomalous variations of spectral linewidth in internal excitonic quantum transitions of ultrafast resonantly excited single-walled carbon nanotubes," *Phys. Rev. Mater.* **3** (2019).
- <sup>52</sup>R. Wood, *Laser Damage in Optical Materials* (IOP Publishing, 1986).
- <sup>53</sup>E. Optics, "Laser Optical Components," (2019).
- <sup>54</sup>L. Liu, P.-C. Ma, M. Xu, S. U. Khan, and J.-K. Kim, "Strain-sensitive Raman spectroscopy and electrical resistance of carbon nanotube-coated glass fibre sensors," *Composites Science and Technology* **72**, 1548–1555 (2012).
- <sup>55</sup>R. Saito, *Physical properties of carbon nanotubes* (Imperial College Press, 1998).
- <sup>56</sup>S. Nanot, N. A. Thompson, J.-H. Kim, X. Wang, W. D. Rice, E. H. Háróz, Y. Ganesan, C. L. Pint, and J. Kono, "Springer Handbook of Nanomaterials," (Springer Berlin Heidelberg, 2013) Chap. 4. Single-Walled Carbon Nanotubes, pp. 105–146.
- <sup>57</sup>A. Jorio, M. S. Dresselhaus, and G. Dresselhaus, eds., *Carbon Nanotubes* (Springer-Verlag GmbH, 2008).
- <sup>58</sup>T. Ando, "Excitons in Carbon Nanotubes," *J. Phys. Soc. Japan* **66**, 1066–1073 (1997).
- <sup>59</sup>T. Ando, "Excitons in Carbon Nanotubes Revisited: Dependence on Diameter, Aharonov–Bohm Flux, and Strain," *J. Phys. Soc. Japan* **73**, 3351–3363 (2004).
- <sup>60</sup>F. Wang, D. J. Cho, B. Kessler, J. Deslippe, P. J. Schuck, S. G. Louie, A. Zettl, T. F. Heinz, and Y. R. Shen, "Observation of Excitons in One-Dimensional Metallic Single-Walled Carbon Nanotubes," *Phys. Rev. Lett.* **99** (2007).
- <sup>61</sup>F. Wang, G. Dukovic, L. E. Brus, and T. F. Heinz, "The Optical Resonances in Carbon Nanotubes Arise from Excitons," *Science* **308**, 838–841 (2005).
- <sup>62</sup>J. Li, Y. Lu, Q. Ye, M. Cinke, J. Han, and M. Meyyappan, "Carbon Nanotube Sensors for Gas and Organic Vapor Detection," *Nano Lett.* **3**, 929–933 (2003).
- <sup>63</sup>B. Liu, F. Wu, H. Gui, M. Zheng, and C. Zhou, "Chirality-Controlled Synthesis and Applications of Single-Wall Carbon Nanotubes," *ACS Nano* **11**, 31–53 (2017).
- <sup>64</sup>J. A. Fagan, B. J. Landi, I. Mandelbaum, J. R. Simpson, V. Bajpai, B. J. Bauer, K. Migler, A. R. H. Walker, R. Raffaele, and E. K. Hobbie, "Comparative measures of single-wall carbon nanotube dispersion," *J. Phys.*

- Chem. B **110**, 23801 (2006).
- <sup>65</sup>V. Amendola, R. Pilot, M. Frascioni, O. M. Maragò, and M. A. Iati, "Surface plasmon resonance in gold nanoparticles: a review," *J. Phys.: Condens. Matt.* **29**, 203002 (2017).
- <sup>66</sup>A.-C. Genix and J. Oberdisse, "Nanoparticle self-assembly: from interactions in suspension to polymer nanocomposites," *Soft Matt.* **14**, 5161 (2018).